DOI: 10.19884/j.1672-5220.202404004

Porous $Ti_3C_2T_x$ for Efficient Electrocatalytic Hydrogen Evolution Reaction

LIU Ying[1], HUI Mingming[1], BU Fanxing[2*], LUO Wei[1*]
1. College of Materials Science and Engineering, Donghua University, Shanghai 201620, China
2. Key Laboratory of Silicate Cultural Relics Conservation, Ministry of Education, School of Cultural Heritage and Information Management, Shanghai University, Shanghai 200444, China

Abstract: MXene is an emerging class of two-dimensional (2D) layered transition metal carbides or nitrides. Due to the highly tunable components and surface functional groups, it holds great potential in electrocatalytic hydrogen evolution reaction (HER). However, MXene nanosheet suffers from a strong tendency to restack and a lack of active edge sites. In this work, the porous $Ti_3C_2T_x$ was synthesized by an oxidation and etching two-step strategy and then characterized by a series of spectroscopic techniques. The obtained porous $Ti_3C_2T_x$ possesses a large number of in-plane pores. This not only creates abundant active edge sites but also enhances the mass transfer and increases the accessibility of the active sites. Compared with $Ti_3C_2T_x$, in a 0.5 mol/L H_2SO_4 electrolyte, the porous $Ti_3C_2T_x$ shows a 65.6% higher electrochemical surface area (ECSA) (440 mF/cm^2), a 95.2% lower charge transfer resistance (12.8 Ω), and a 69.8% lower Tafel slope (144 mV/dec), and thus exhibits lower overpotential with good stability at a current density of 10 mA/cm^2. At the same time, the HER performance of the porous $Ti_3C_2T_x$ can be further enhanced by near-infrared laser irradiation based on the localized surface plasmon resonance effect.

Keywords: porous $Ti_3C_2T_x$; hydrogen evolution reaction (HER); active edge site; localized surface plasmon resonance
CLC number: O611 **Document code**: A
Article ID: 1672-5220(2025)01-0020-09

Open Science Identity (OSID)

0 Introduction

Hydrogen is a renewable and green energy source, serving as a potential alternative to traditional fossil fuels, meeting the demands of sustainable social development[1]. Electrochemical water splitting via the hydrogen evolution reaction (HER) is considered as the most economical and efficient method for hydrogen production[2]. Pt-based noble metal materials have attracted great attention due to their efficient HER performance[3-5], but high cost and scarcity hinder their large-scale applications[6]. Therefore, the rational design of economically efficient HER electrocatalysts is an important research topic at present[7-9]. MXene is an emerging class of two-dimensional (2D) layered transition metal carbides or nitrides[10-12] with excellent conductivity[13], highly tunable composition[14] and surface functional groups[15], holding great potential in HER[16]. However, MXene nanosheet has a high aspect ratio structure, which mainly exposes in-plane sites with poor activity, leading to poor intrinsic activity[17-18]. Moreover, due to the strong van der Waals forces between 2D nanosheets[19], MXene tends to restack[20-21], which hinders ion transport and reduces the accessibility of active sites, further degrading its electrochemical performance[22]. Therefore, enhancing the HER performance of the MXene materials is an urgent task[23-24].

Recently, MXene nanofibers[25] and MXene quantum dots have been developed as efficient HER catalysts. Electrochemical analysis reveals that the edge sites of MXene possess a different coordination environment from the in-plane sites, which exhibit a more optimized electronic structure in HER, reducing the reaction barrier and significantly enhancing the intrinsic activity of MXene. Additionally, Wu et al.[26] found that MXene possesses localized surface plasmon resonance effects in the visible-near-infrared spectral region. The resulting intense photothermal effect and hot-electron injection reduce the endothermic enthalpy, activation energy and interfacial charge transfer resistance of HER, and thus significantly improve the HER performance. Therefore, designing MXene materials with a large number of exposed active edge sites and modulating them with external physical fields is an effective way to enhance their HER performance.

This work reports an in-plane pore engineering strategy to enhance the HER performance of $Ti_3C_2T_x$. The porous $Ti_3C_2T_x$ is synthesized by an oxidation and etching two-step strategy. The generation of a large number of in-plane pores increases active edge sites, enhances the mass transfer and also improves the

Received date: 2024-04-03
Foundation item: National Outstanding Youth Science Foundation (No. 52225204)
* Correspondence should be addressed to LUO Wei, email: wluo@dhu.edu.cn; BU Fanxing, email: fxbu@shu.edu.cn
Citation: LIU Y, HUI M M, BU F X, et al. Porous $Ti_3C_2T_x$ for efficient electrocatalytic hydrogen evolution reaction [J]. *Journal of Donghua University (English Edition)*, 2025, 42(1): 20-28.

accessibility of active sites, synergistically enhancing the HER performance of the porous $Ti_3C_2T_x$. Moreover, benefiting from the localized surface plasmon resonance effect of $Ti_3C_2T_x$, its HER performance is further enhanced under near-infrared laser irradiation.

1 Materials and Methods

1.1 Materials

Ti_3AlC_2, dimethyl sulfoxide (DMSO) and LiF were supplied by Adamas Pharmaceuticals Inc., USA. $CuSO_4 \cdot 5H_2O$ and Nafion were purchased from Sigma-Aldrich (Shanghai) Trading Co., Ltd., USA. H_2O_2, HF, HCl and other routine chemicals were supplied by Shanghai Hushi Laboratorial Equipment Co., Ltd., China.

1.2 Synthesis of $Ti_3C_2T_x$

$Ti_3C_2T_x$ was synthesized by the modified minimally intensive layer delamination (MILD) method[17]. First, 2.5 g Ti_3AlC_2 and 4 g LiF were added to a sealed polytetrafluoroethylene bottle. Then 50 mL HCl (9 mol/L) was slowly added to the above solution within 10 min to alleviate the initial overheating reaction. The reaction system was successively transferred to a 35 ℃ oil bath and then stirred for 24 h. The etched $Ti_3C_2T_x$ was washed with a large amount of water to remove acid, metal ions and LiF until the pH value of the supernatant reached 7. Subsequently, the obtained $Ti_3C_2T_x$ precipitation was added to a solution composed of 30 mL H_2O and 200 mL DMSO. Later, the resulting $Ti_3C_2T_x$ colloidal solution was centrifuged and washed with water twice. Then, the obtained $Ti_3C_2T_x$ colloidal dispersion was subjected to centrifugation at 3 500 r/min for 40 min to remove any aggregates. Finally, the obtained $Ti_3C_2T_x$ solution with a mass concentration of 39 mg/mL was collected and stored at 4 ℃ for the following experiments.

1.3 Synthesis of porous $Ti_3C_2T_x$

The porous $Ti_3C_2T_x$ was synthesized via the oxidation and etching two-step strategy reported by our group[17]. Firstly, 120 μL $CuSO_4$ solution (1 mol/L) and 60 μL H_2O_2 were added into $Ti_3C_2T_x$ solution (1.54 mL) and stirred for 30 min to obtain $Ti_3C_2T_x/TiO_2$ composites. Subsequently, the obtained $Ti_3C_2T_x/TiO_2$ composites were collected by centrifugation, washed with water three times and then dispersed into 60 mL water. Then 8 mL HF was added to fully remove TiO_2. Finally, after stirring for 30 min, the products were collected by centrifugation and washed with water three times.

1.4 Material characterizations

Transmission electron microscopy (TEM) images were taken on a microscope (JEOL2100F, JEOL Ltd., Japan) at a voltage of 200 kV. X-ray diffraction (XRD) patterns were obtained using a powder X-ray diffractometer (D8, Bruker, Germany). Fourier transform infrared (FTIR) spectra were recorded using a spectrometer (Nicolet 7000-C, Thermo Fisher, USA) with the KBr pellet method. X-ray photoelectron spectroscopy (XPS) measurements were performed on an XPS spectrometer (Escalab250Xi, Thermo Fisher, USA). Ultraviolet-visible (UV-Vis) absorption spectra were acquired using a UV-Vis spectrometer (UV-1900i, Shimadzu, Japan).

1.5 Electrochemical measurements

The electrochemical measurements were conducted with an electrochemical workstation (Model636A, Princeton Applied Research, USA). The working electrode was prepared by dropping a certain amount of catalyst slurry onto the glassy carbon electrode. The catalyst slurry was prepared as follows. The product (5 mg) was added to the mixture of 950 μL ethanol and 50 μL Nafion, followed by ultrasonication for 30 min to disperse the catalyst evenly. Then, the catalyst slurry (12 μL) was dropped onto the glassy carbon electrode by a pipetting gun to obtain the catalyst loading at 0.3 mg/cm^2. By changing the catalyst slurry amount, the catalyst with different loadings including 0.1, 0.2, 0.3 and 0.5 mg/cm^2 was fabricated for the electrochemical measurements. The corresponding porous $Ti_3C_2T_x$ samples were denoted as porous $Ti_3C_2T_x$-0.1, porous $Ti_3C_2T_x$-0.2, porous $Ti_3C_2T_x$-0.3 and porous $Ti_3C_2T_x$-0.5, respectively. The cyclic voltammetry (CV) was recorded with a scanning rate of 50 mV/s for several cycles until it was stable. In all measurements, linear sweep voltammetry (LSV) tests were carried out with internal resistance compensation, and the presented potential values were calibrated to a reversible hydrogen electrode (RHE).

$$E_{RHE} = E_{Ag/AgCl} + 0.197 + 0.059 \times pH,$$

where E_{RHE} is the electrode potential against RHE; $E_{Ag/AgCl}$ is the applied potential against the Ag/AgCl electrode.

The stability of the catalyst was characterized using a chronoamperometry method at a current density of 10 mA/cm^2. Electrochemical impedance spectroscopy (EIS) was implemented in a frequency range of 0.1 to 105.0 Hz. From the above measurement data, the corresponding double-layer capacitance, electrochemical surface area (ECSA) and Tafel slope were calculated.

To evaluate the influence of the localized surface plasmon resonance effect on HER performance, an infrared light was fixed at 5 cm from the electrode, and an 808 nm near-infrared laser was used to irradiate the surface of the catalyst at a laser power of 5 W to test its HER performance in different electrolyte environments.

2 Results and Discussion

2.1 Morphological analysis of $Ti_3C_2T_x$ and porous $Ti_3C_2T_x$

TEM images (Fig. 1) demonstrate that $Ti_3C_2T_x$, $Ti_3C_2T_x/TiO_2$ and the porous $Ti_3C_2T_x$ present ultrathin 2D layered structures. $Ti_3C_2T_x$ nanosheets are smooth and flat (Fig. 1(a)). By contrast, TiO_2 quantum dots are uniformly inlaid across the whole $Ti_3C_2T_x$ nanosheets (Fig. 1(b)). With further etching, densely distributed nanopores throughout the nanosheets are viewed on the surface of the porous $Ti_3C_2T_x$ (Fig. 1(c)), indicating the successful fabrication of in-plane pores.

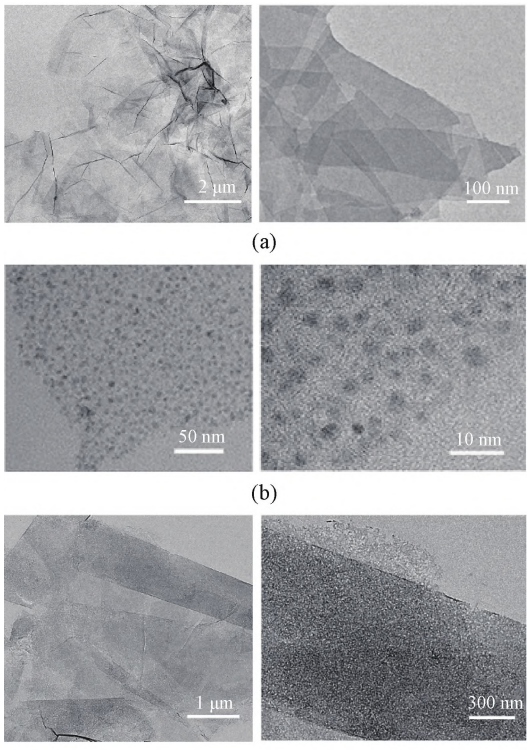

Fig. 1 TEM images of samples at different magnifications: (a) $Ti_3C_2T_x$; (b) $Ti_3C_2T_x/TiO_2$; (c) porous $Ti_3C_2T_x$

2.2 Structural analysis of $Ti_3C_2T_x$ and porous $Ti_3C_2T_x$

The XRD pattern (Fig. 2) of $Ti_3C_2T_x$ presents several characteristic diffraction peaks corresponding to (002), (004), (006), (008), (0010) and (0012) crystal planes, which are attributed to the stacking of 2D nanosheets. In comparison, the porous $Ti_3C_2T_x$ only exhibits one obvious characteristic diffraction peak corresponding to (002) crystal plane. Furthermore, this peak exhibits a leftward shift, indicating an increased interlayer spacing in the porous $Ti_3C_2T_x$[27].

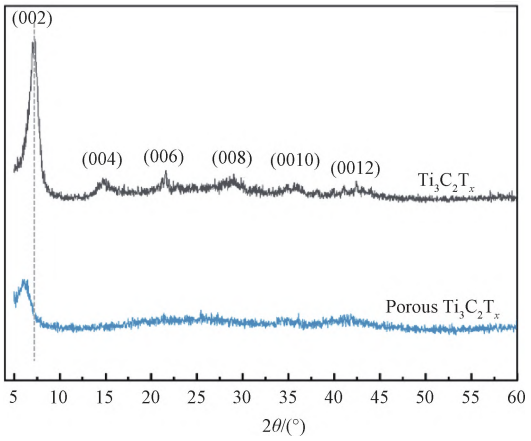

Fig. 2 XRD patterns of $Ti_3C_2T_x$ and porous $Ti_3C_2T_x$

The FTIR spectra of $Ti_3C_2T_x$ and the porous $Ti_3C_2T_x$ (Fig. 3) exhibit peaks at 1 000–1 500 cm^{-1} and 2 800–3 700 cm^{-1}, corresponding to the characteristic peaks of the C—C bonds and the O—H bonds, respectively. The peak at 1650 – 1 750 cm^{-1} corresponds to the C═O bonds. Those similar peaks indicate the oxidation and etching treatments do not obviously change the surface functional groups.

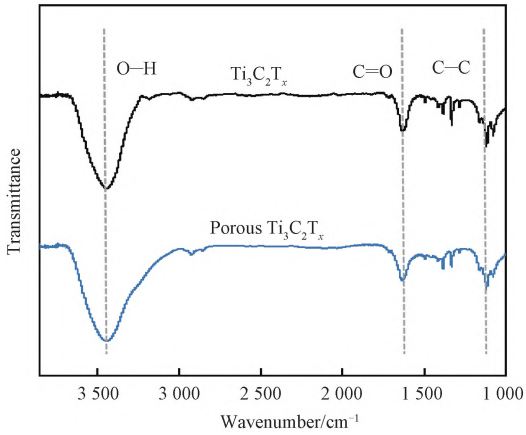

Fig. 3 FTIR spectra of $Ti_3C_2T_x$ and porous $Ti_3C_2T_x$

The XPS spectra of $Ti_3C_2T_x$ (Fig. 4(a)) and the porous $Ti_3C_2T_x$ (Fig. 4(b)) show that both materials contain Ti, C, O, Cl and F elements. Ti^+, Ti^{2+}, Ti^{3+} and Ti^{4+} species are observed in the Ti 2p XPS spectra of $Ti_3C_2T_x$ (Fig. 4(c)) and the porous $Ti_3C_2T_x$ (Fig. 4(d)), which can be assigned to Ti atoms bound to terminal oxygen-containing groups, Ti atoms bound to OH terminals, Ti atoms in $Ti_3C_2OH \cdot H_2O$ complexes, and Ti atoms in TiO_2, respectively. In comparison with $Ti_3C_2T_x$, the porous $Ti_3C_2T_x$ exhibits a significant increase in Ti^{4+} content, indicating the formation of more TiO_2. The reason is that the porous $Ti_3C_2T_x$ possesses more edge sites and a larger surface area, which facilitates the oxidation of $Ti_3C_2T_x$. This result indicates that the porous $Ti_3C_2T_x$ enhances the intrinsic activity of $Ti_3C_2T_x$.

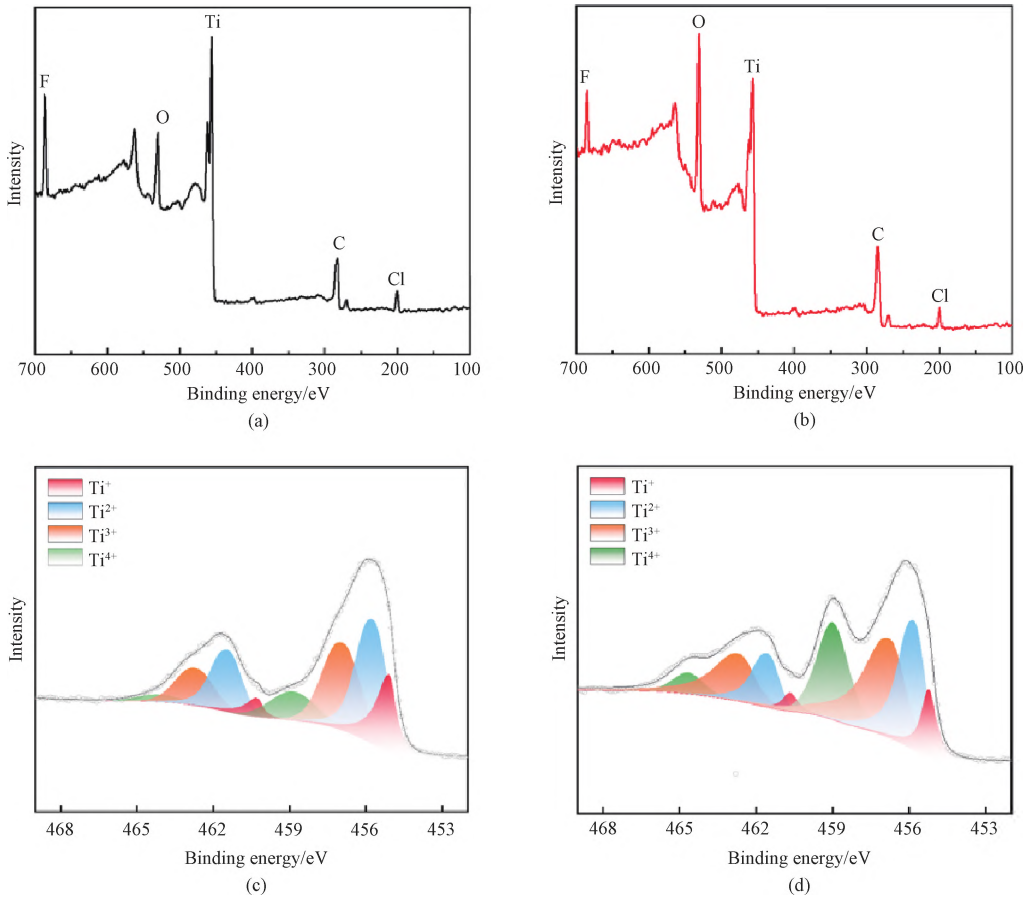

Fig. 4 XPS spectra: (a) full XPS spectrum of $Ti_3C_2T_x$; (b) full XPS spectrum of porous $Ti_3C_2T_x$; (c) Ti 2p XPS spectrum of $Ti_3C_2T_x$; (d) Ti 2p XPS spectrum of porous $Ti_3C_2T_x$

The UV-Vis spectra (Fig. 5) present that the porous $Ti_3C_2T_x$ at different mass concentrations (20, 60 and 100 μg/mL) all exhibit a broad and strong plasma absorption band centered at 820 nm, consistent with the results in previous reports[28]. According to Lambert-Beer law, the extinction coefficient of the porous $Ti_3C_2T_x$ is calculated to be 20.75 L/(g·cm), significantly higher than that of the reported photothermal agents at similar wavelengths[29-32]. This indicates that the porous $Ti_3C_2T_x$ also exhibits a significant local surface plasmon resonance effect, which can generate substantial photothermal conversion and thermal electron implantation effects under 808 nm near-infrared laser irradiation, and then greatly enhance its electrocatalytic HER performance.

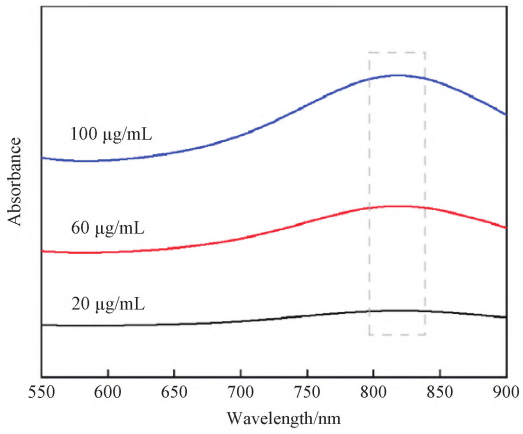

Fig. 5 UV-Vis spectra of porous $Ti_3C_2T_x$ at different mass concentrations

2.3 HER performance testing and analysis

Figure 6 shows the effect of the porous $Ti_3C_2T_x$ loading on HER performance. The overpotentials (at 10 mA/cm^2) for different loadings of 0.1, 0.2, 0.3 and 0.5 mg/cm^2 are 660, 600, 540 and 550 mV, respectively. It can be seen that with the increase of catalyst loading, the catalytic performance increases and then decreases, and the best HER performance was obtained at 0.3 mg/cm^2. It is possible that with low loading, the catalyst is not enough to cover the whole working electrode, causing insufficient active sites and resulting in degraded performance. In contrast, high loading leads to over-stacking of catalysts, reducing proton transport efficiency and also leading to deteriorated performance. Therefore, the catalyst loading used in this work is determined as 0.3 mg/cm^2.

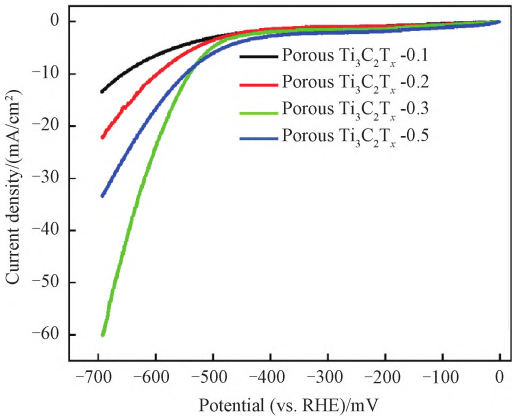

Fig. 6 LSV curves of porous $Ti_3C_2T_x$ at different loadings in 0.5 mol/L H_2SO_4

The HER performances of $Ti_3C_2T_x$ and the porous $Ti_3C_2T_x$ were further evaluated in different electrolyte environments[33]. LSV curves of $Ti_3C_2T_x$ and the porous $Ti_3C_2T_x$ in 0.1 mol/L $HClO_4$, 0.1 mol/L KOH, 0.05 mol/L H_2SO_4 and 0.5 mol/L H_2SO_4 are shown in Fig. 7. The porous $Ti_3C_2T_x$ shows the best HER performance in 0.5 mol/L H_2SO_4 with a current density of 26 mA/cm² at the 600 mV overpotential. However, only 10.2, 6.7 and 7.9 mA/cm² can be reached in 0.1 mol/L $HClO_4$, 0.1 mol/L KOH and 0.05 mol/L H_2SO_4, respectively. Moreover, the HER performance of the porous $Ti_3C_2T_x$ is better than that of $Ti_3C_2T_x$ in all these four electrolyte environments.

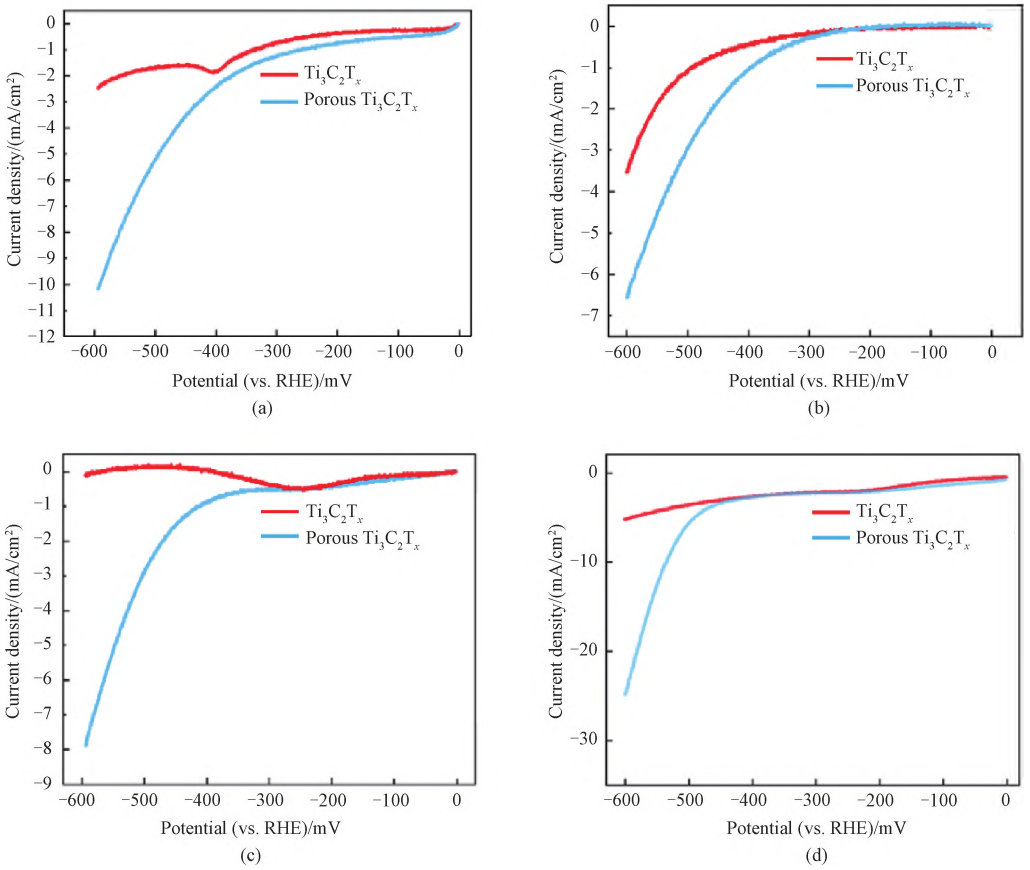

Fig. 7 LSV curves of $Ti_3C_2T_x$ and porous $Ti_3C_2T_x$ in different electrolyte environments: (a) 0.1 mol/L $HClO_4$; (b) 0.1 mol/L KOH; (c) 0.05 mol/L H_2SO_4; (d) 0.5 mol/L H_2SO_4

To investigate the operational stability of the porous $Ti_3C_2T_x$ in 0.5 mol/L H_2SO_4, a long-term stability test was conducted at a current density of 10 mA/cm². As shown in Fig. 8, due to the electrolyte wetting and catalyst activation process, the overpotential of the porous $Ti_3C_2T_x$ shows a slight decrease in the initial stage and then stabilizes to operate over 20 000 s. The overpotentials of the porous $Ti_3C_2T_x$ before and after activation were recorded as 569 mV and 530 mV, which were still superior to those of $Ti_3C_2T_x$ (653 mV and 601 mV). Hence, the formation of in-plane pores in porous $Ti_3C_2T_x$ did not compromise the stability of its electrochemical HER.

To understand the better HER performance of the porous $Ti_3C_2T_x$ compared to $Ti_3C_2T_x$, the CV curves of $Ti_3C_2T_x$ (Fig. 9(a)) and the porous $Ti_3C_2T_x$ (Fig. 9(b)) were measured at different scanning rates. The potential range was set within an interval of 0 – 100 mV (vs. RHE).

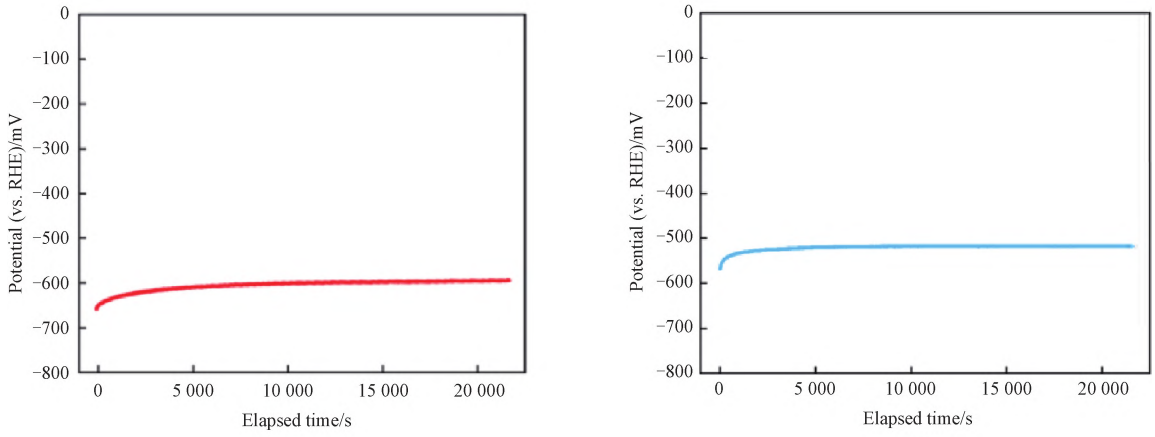

Fig. 8 Potential-elapsed time curves of samples in 0.5 mol/L H_2SO_4: (a) $Ti_3C_2T_x$; (b) porous $Ti_3C_2T_x$

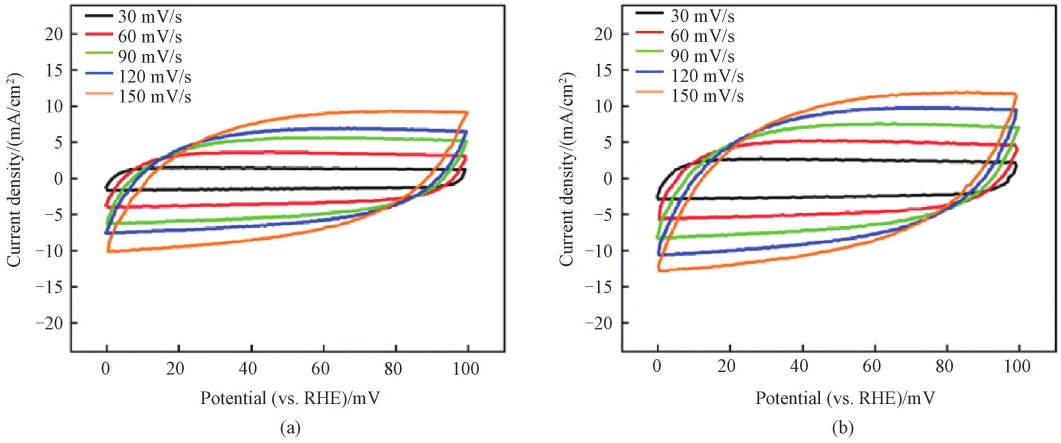

Fig. 9 CV curves of samples in 0.5 mol/L H_2SO_4 at different scanning rates in potential range of 0−100 mV (vs. RHE): (a) $Ti_3C_2T_x$; (b) porous $Ti_3C_2T_x$

The linear fitting curves of the capacitive current density at 50 mV (vs. RHE) as a function of CV scanning rate are shown in Fig. 10. The double-layer capacitance of the porous $Ti_3C_2T_x$ is 15.4 mF and that of $Ti_3C_2T_x$ is 9.3 mF. Furthermore, the ECSA of the porous $Ti_3C_2T_x$ at 50 mV (vs. RHE) is 440.0 mF/cm^2 (Fig. 11), which is 65.6% higher than that of $Ti_3C_2T_x$ (265.7 mF/cm^2). This indicates that the porous $Ti_3C_2T_x$ possesses a larger ECSA and more active sites compared to $Ti_3C_2T_x$.

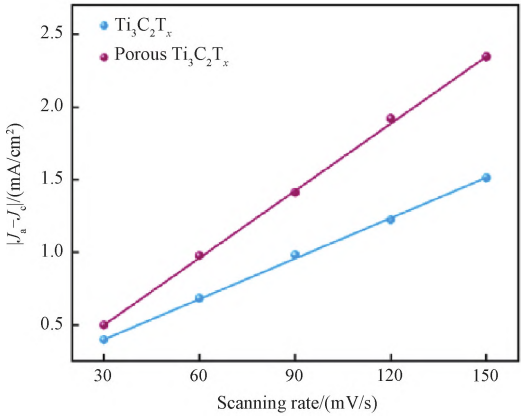

Fig. 10 Linear fitting curves of capacitive current density $|J_a-J_c|$ as a function of CV scanning rate (J_a is anodic current density; J_c is cathodic current density)

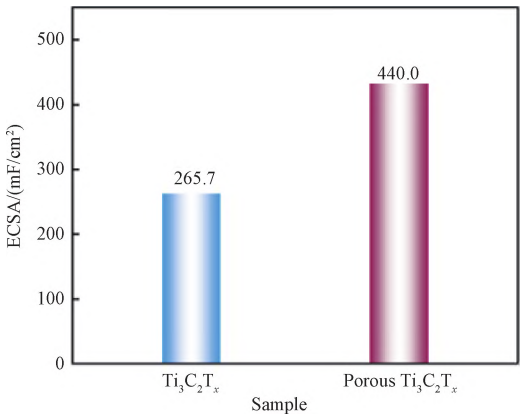

Fig. 11 ECSA values of $Ti_3C_2T_x$ and porous $Ti_3C_2T_x$ at 50 mV (vs. RHE)

The Tafel slope curves of the catalysts were also simulated (Fig. 12). The Tafel slope of the porous $Ti_3C_2T_x$ is 144 mV/dec, which is 69.8% lower than that of $Ti_3C_2T_x$ (477 mV/dec), suggesting superior HER kinetics for the porous $Ti_3C_2T_x$ compared to $Ti_3C_2T_x$.

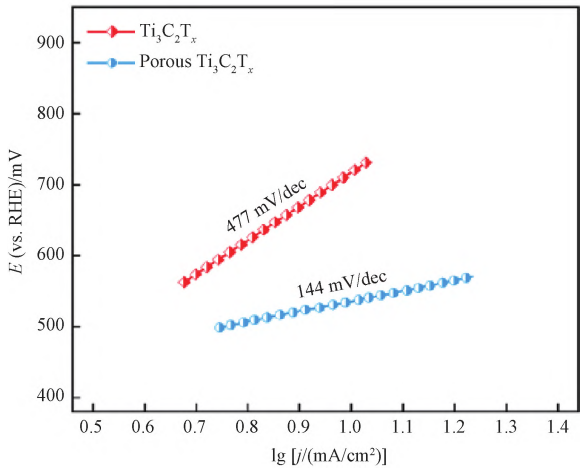

Fig. 12 Tafel slope curves of $Ti_3C_2T_x$ and porous $Ti_3C_2T_x$ in 0.5 mol/L H_2SO_4 (E is potential; j is current density)

Furthermore, the EIS technique was employed to investigate the interfacial reaction and kinetic process of the electrode during the HER process (Fig. 13). The radius of the EIS curve for the porous $Ti_3C_2T_x$ (12.8 Ω) is notably smaller than that for $Ti_3C_2T_x$ (265.0 Ω), indicating that the porous $Ti_3C_2T_x$ has smaller charge transfer resistance and faster reaction kinetics. These results collectively demonstrate that the introduction of in-plane pores in porous $Ti_3C_2T_x$ can enhance its HER catalytic activity.

At last, the influence of localized surface plasmon resonance effect on the HER performance of the porous $Ti_3C_2T_x$ in 0.5 mol/L H_2SO_4 was evaluated by irradiating the surface of the working electrodes with an 808 nm near-infrared laser lamp. It was found that along with the increase of the laser power, the HER performances of both $Ti_3C_2T_x$ and the porous $Ti_3C_2T_x$ improved (Fig. 14). Notably, when the overpotential reached 700 mV, the current density of $Ti_3C_2T_x$ at a laser power of 5 W was near 50 mA/cm^2, whereas the current density of the porous $Ti_3C_2T_x$ at a laser power of 5 W achieved 80 mA/cm^2. These results suggest that both $Ti_3C_2T_x$ and the porous $Ti_3C_2T_x$ exhibit localized surface plasmon resonance effects. However, due to its more active edge sites and larger specific surface area, the porous $Ti_3C_2T_x$ exhibits better HER performance.

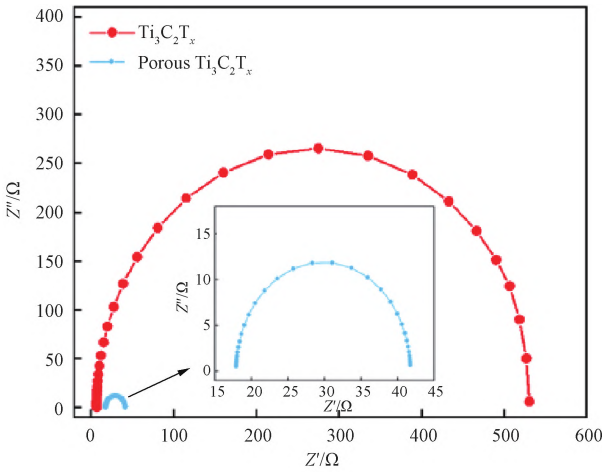

Fig. 13 EIS curves of $Ti_3C_2T_x$ and porous $Ti_3C_2T_x$ in 0.5 mol/L H_2SO_4 (Z' is real part of impedance; Z'' is imaginary part of impedance)

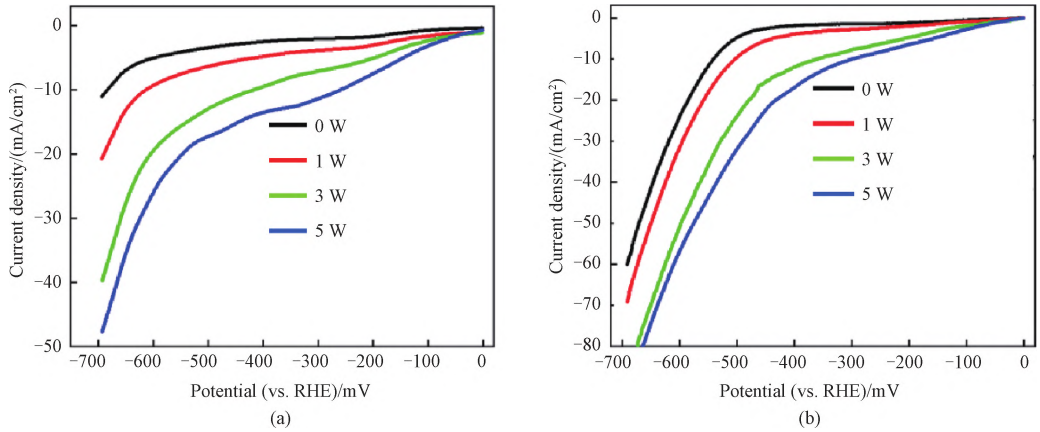

Fig. 14 LSV curves of samples in 0.5 mol/L H_2SO_4 at different laser powers: (a) $Ti_3C_2T_x$; (b) porous $Ti_3C_2T_x$

3 Conclusions

In this work, we report an in-plane pore engineering strategy to enhance the HER performance of $Ti_3C_2T_x$. The porous $Ti_3C_2T_x$ was synthesized by an oxidation and etching two-step strategy, and the micro-morphology and electrochemical properties were characterized. The obtained porous $Ti_3C_2T_x$ possesses a large number of in-plane pores. This not only creates a large number of active edge sites, but also enhances the mass transfer and improves the accessibility of the active sites, greatly

enhancing the electrocatalytic HER performance. Compared to $Ti_3C_2T_x$, the porous $Ti_3C_2T_x$ shows a higher ECSA (440 mF/cm^2), a lower charge EIS (12.8 Ω) and a lower Tafel slope (144 mV/dec), and thus exhibits lower overpotential with good stability at a current density of 10 mA/cm^2. Meanwhile, the localized surface plasmon resonance effect can be exploited to further enhance the electrocatalytic HER performance of the porous $Ti_3C_2T_x$ under near-infrared laser irradiation. This work provides a novel strategy to enhance the electrocatalytic HER performance of MXene.

References

[1] WU R, XU J, ZHAO C L, et al. Dopant triggered atomic configuration activates water splitting to hydrogen[J]. *Nature Communications*, 2023, 14: 2306.

[2] TURNER J A. Sustainable hydrogen production [J]. *Science*, 2004, 305(5686): 972-974.

[3] WEI J X, XIAO K, CHEN Y X, et al. In situ precise anchoring of Pt single atoms in spinel Mn_3O_4 for a highly efficient hydrogen evolution reaction[J]. *Energy & Environmental Science*, 2022, 15(11): 4592-4600.

[4] YANG L, GRZESCHIK R, JIANG P, et al. Tuning the electronic properties of platinum in hybrid-nanoparticle assemblies for use in hydrogen evolution reaction [J]. *Angewandte Chemie International Edition*, 2023, 62(25): e202301065.

[5] CHEN Y W, DING R, LI J, et al. Highly active atomically dispersed platinum-based electrocatalyst for hydrogen evolution reaction achieved by defect anchoring strategy [J]. *Applied Catalysis B: Environmental*, 2022, 301: 120830.

[6] MCCRORY C C L, JUNG S, FERRER I M, et al. Benchmarking hydrogen evolving reaction and oxygen volving reaction electrocatalysts for solar water splitting devices[J]. *Journal of the American Chemical Society*, 2015, 137(13): 4347-4357.

[7] WANG X M, LONG G F, LIU B, et al. Rationally modulating the functions of Ni_3Sn_2-$NiSnO_x$ nanocomposite electrocatalysts towards enhanced hydrogen evolution reaction [J]. *Angewandte Chemie International Edition*, 2023, 62(19): e202301562.

[8] DING R, CHEN Y W, LI X K, et al. Atomically dispersed, low-coordinate Co–N sites on carbon nanotubes as inexpensive and efficient electrocatalysts for hydrogen evolution [J]. *Small*, 2022, 18(4): 2105335.

[9] ZHANG L H, GUO X Y, ZHANG S L, et al. Hybrid double atom catalysts for hydrogen evolution reaction: a sweet marriage of metal and nonmetal [J]. *Advanced Energy Materials*, 2024, 14(2): 2302754.

[10] RONG C, SU T, LI Z K, et al. Elastic properties and tensile strength of 2D $Ti_3C_2T_x$ MXene monolayers[J]. *Nature Communications*, 2024, 15: 1566.

[11] VAHIDMOHAMMADI A, ROSEN J, GOGOTSI Y. The world of two-dimensional carbides and nitrides (MXenes) [J]. *Science*, 2021, 372 (6547): eabf1581.

[12] BI W C, GAO G H, LI C, et al. Synthesis, properties, and applications of MXenes and their composites for electrical energy storage [J]. *Progress in Materials Science*, 2024, 142: 101227.

[13] LEE C, PARK S M, KIM S, et al. Field-induced orientational switching produces vertically aligned $Ti_3C_2T_x$ MXene nanosheets[J]. *Nature Communications*, 2022, 13: 5615.

[14] ZHANG T Z, CHANG L B, ZHANG X F, et al. Simultaneously tuning interlayer spacing and termination of MXenes by Lewis-basic halides[J]. *Nature Communications*, 2022, 13: 6731.

[15] SHIMADA T, TAKENAKA N, ANDO Y, et al. Relationship between electric double-layer structure of MXene electrode and its surface functional groups[J]. *Chemistry of Materials*, 2022, 34(5): 2069-2075.

[16] KAZIM S, HUANG C, HEMASIRI N H, et al. MXene-based energy devices: from progressive to prospective[J]. *Advanced Functional Materials*, 2024, 34(50): 2315694.

[17] BU F X, SUN Z H, ZHOU W H, et al. Reviving Zn^0 dendrites to electroactive Zn^{2+} by mesoporous MXene with active edge sites[J]. *Journal of the American Chemical Society*, 2023, 145(44): 24284-24293.

[18] JIANG B W, YANG T, WANG T T, et al. Edge stimulated hydrogen evolution reaction on monodispersed MXene quantum dots [J]. *Chemical Engineering Journal*, 2022, 442: 136119.

[19] ZHU J Y, LI F, HOU Y Z, et al. Near-room-temperature water-mediated densification of bulk van der Waals materials from their nanosheets [J]. *Nature Materials*, 2024, 23: 604-611.

[20] ZHAO R Z, ELZATAHRY A, CHAO D L, et al. Making MXenes more energetic in aqueous battery[J]. *Matter*, 2022, 5(1): 8-10.

[21] WU Y C, WEI W, YU R H, et al. Anchoring sub-nanometer Pt clusters on crumpled paper-like MXene enables high hydrogen evolution mass activity [J]. *Advanced Functional Materials*, 2022, 32(17): 2110910.

[22] ZHU Y C, RAJOU Â K, LE VOT S, et al.

Modifications of MXene layers for supercapacitors [J]. *Nano Energy*, 2020, 73: 104734.
[23] PENG J H, ZHANG Z Y, WANG H, et al. Amorphization of MXenes: boosting electrocatalytic hydrogen evolution [J]. *Small*, 2024, 20(16): 2308528.
[24] GU Y T, WEI B, LEGUT D, et al. Single atom-modified hybrid transition metal carbides as efficient hydrogen evolution reaction catalysts [J]. *Advanced Functional Materials*, 2021, 31(43): 2104285.
[25] YUAN W Y, CHENG L F, AN Y R, et al. MXene nanofibers as highly active catalysts for hydrogen evolution reaction [J]. *ACS Sustainable Chemistry & Engineering*, 2018, 6(7): 8976-8982.
[26] WU X H, WANG J H, WANG Z Y, et al. Boosting the electrocatalysis of MXenes by plasmon-induced thermalization and hot-electron injection [J]. *Angewandte Chemie International Edition*, 2021, 60(17): 9416-9420.
[27] PENG M K, WANG L, LI L B, et al. Manipulating the interlayer spacing of 3D MXenes with improved stability and zinc-ion storage capability [J]. *Advanced Functional Materials*, 2022, 32(7): 2109524.
[28] WANG D B, FANG Y X, YU W, et al. Significant solar energy absorption of MXene $Ti_3C_2T_x$ nanofluids via localized surface plasmon resonance [J]. *Solar Energy Materials and Solar Cells*, 2021, 220: 110850.
[29] LIAN Z, WU F, ZI J, et al. Infrared light-induced anomalous defect-mediated plasmonic hot electron transfer for enhanced photocatalytic hydrogen evolution [J]. *Journal of the American Chemical Society*, 2023, 145(28): 15482-15487.
[30] CHEN J, FENG J, YANG F, et al. Space-confined seeded growth of Cu nanorods with strong surface plasmon resonance for photothermal actuation [J]. *Angewandte Chemie International Edition*, 2019, 58(27): 9275-9281.
[31] WU S, ZHANG P, JIANG Z, et al. Enhanced peroxidase-like activity of CuS hollow nanocages by plasmon-induced hot carriers and photothermal effect for the dual-mode detection of tannic acid [J]. *ACS Applied Materials & Interfaces*, 2022, 14(35): 40191-40199.
[32] JIAO S L, DAI K, BESTEIRO L V, et al. Differentiating plasmon-enhanced chemical reactions on AgPd hollow nanoplates through surface-enhanced Raman spectroscopy [J]. *ACS Catalysis*, 2024, 14(9): 6799-6806.
[33] MA T T, WANG P, NIU H J, et al. Single Ru atoms dispersed on $MoSe_2$/MXene nanosheets with multiple interfaces for enhanced acidic hydrogen evolution [J]. *Carbon*, 2024, 218: 118758.

多孔 $Ti_3C_2T_x$ 用于高效电催化析氢反应

刘　影[1]，惠明明[1]，卜凡兴[2*]，罗　维[1*]

1. 东华大学 材料科学与工程学院，上海 201620
2. 上海大学 文化遗产与信息管理学院 硅酸盐质文物保护教育部重点实验室，上海 200444

摘　要： MXene 是一种新兴的二维过渡金属碳化物或氮化物，具有高度可调控的组分和表面官能团，在电催化析氢反应中表现出良好的应用前景，但是 MXene 纳米片极易堆叠且缺乏活性边缘位点。该研究通过氧化和刻蚀两步策略合成了多孔 $Ti_3C_2T_x$，并采用一系列光谱学方法进行了表征。研究发现多孔 $Ti_3C_2T_x$ 表面存在大量面内孔，这不仅增加了大量活性边缘位点，而且提高了活性位点的可及性。相比于 $Ti_3C_2T_x$，多孔 $Ti_3C_2T_x$ 在 0.5 mol/L H_2SO_4 电解质中的电化学活性比表面积(440 mF/cm^2)提高 65.6%，电荷转移电阻(12.8 Ω)降低了 95.2%，塔菲尔斜率(144 mV/dec)降低了 69.8%，因此在电流密度为 10 mA/cm^2 时表现出了更低的过电位，且具有很好的稳定性。同时，利用 $Ti_3C_2T_x$ 的局域表面等离子体共振效应，可在近红外激光辐照下进一步提升多孔 $Ti_3C_2T_x$ 的电催化析氢反应性能。

关键词： 多孔 $Ti_3C_2T_x$；析氢反应；活性边缘位点；局域表面等离子体共振效应